Article

Forward modeling of standing kink modes in coronal loops. I. Synthetic views

Yuan, Ding and Doorsselaere, T.V

FORWARD MODELING OF STANDING KINK MODES IN CORONAL LOOPS. I. SYNTHETIC VIEWS

Ding Yuan[1,2,3] and Tom Van Doorsselaere[1]
[1] Centre for Mathematical Plasma Astrophysics, Department of Mathematics, KU Leuven, Celestijnenlaan 200B bus 2400,
B-3001 Leuven, Belgium; DYuan2@uclan.ac.uk
[2] Jeremiah Horrocks Institute, University of Central Lancashire, Preston PR1 2HE, UK
[3] Key Laboratory of Solar Activity, National Astronomical Observatories, Chinese Academy of Sciences, Beijing, 100012, China

ABSTRACT

Kink magnetohydrodynamic (MHD) waves are frequently observed in various magnetic structures of the solar atmosphere. They may contribute significantly to coronal heating and could be used as a tool to diagnose the solar plasma. In this study, we synthesize the Fe IX λ171.073 Å emission of a coronal loop supporting a standing kink MHD mode. The kink MHD wave solution of a plasma cylinder is mapped into a semi-torus structure to simulate a curved coronal loop. We decompose the solution into a quasi-rigid kink motion and a quadrupole term, which dominate the plasma inside and outside of the flux tube, respectively. At the loop edges, the line of sight integrates relatively more ambient plasma, and the background emission becomes significant. The plasma motion associated with the quadrupole term causes spectral line broadening and emission suppression. The periodic intensity suppression will modulate the integrated intensity and the effective loop width, which both exhibit oscillatory variations at half of the kink period. The quadrupole term can be directly observed as a pendular motion at the front view.

Key words: magnetohydrodynamics (MHD) – Sun: atmosphere – Sun: corona – Sun: oscillations – waves

Supporting material: animations

1. INTRODUCTION

In the past decade, significant progress has been achieved in probing the heating and seismological roles of magnetohydrodynamic (MHD) waves in the solar atmosphere (see reviews by Nakariakov & Verwichte 2005; Liu & Ofman 2014; Arregui 2015; Jess et al. 2015). Among the MHD wave modes, the slow magnetoacoustic mode propagates anisotropically in a low β uniform plasma; the wave energy flows predominantly along the magnetic field line, e.g., De Moortel et al. (2002a, 2002b), Wang et al. (2009a, 2009b), Yuan & Nakariakov (2012), Kumar et al. (2013, 2015), and Fang et al. (2015). Meanwhile, a fast magnetoacoustic mode could propagate to any direction relative to the magnetic field, i.e., either parallel, perpendicular, or oblique, therefore they are commonly waveguided in a variety of magnetic structures through reflections and refractions. They may couple with Alfvén waves and exhibit mixed wave properties in forms of standing transverse oscillations of coronal loops (Aschwanden & Schrijver 2011; Nisticò et al. 2013; Verwichte et al. 2013a); large-scale coronal propagating fronts across the whole solar disk (Ofman & Thompson 2002; Liu et al. 2010; Guo et al. 2015); quasi-periodic fast wave trains along magnetic funnels (Liu et al. 2012; Pascoe et al. 2013; Yuan et al. 2013; Nisticò et al. 2014b); fast wave pulses across randomly structured plasma (Yuan et al. 2015a); ubiquitous propagating kink waves in the entire corona (Tomczyk et al. 2007) and coronal holes (Thurgood et al. 2014; Morton et al. 2015).

Kink waves (the $m = 1$ mode, Edwin & Roberts 1982, 1983; Ruderman 2003; Erdélyi & Morton 2009; Goossens et al. 2014) were initially observed in active region loops in the Extreme Ultraviolet (EUV) channels of the Transition Region and Coronal Explorer (TRACE, Aschwanden et al. 1999; Nakariakov et al. 1999). The coronal loops were observed to oscillate transversely with amplitudes at a megameter scale in response to flares, i.e., the associated mass ejections (Schrijver

et al. 2002; Zimovets & Nakariakov 2015), filament destabilizations (Schrijver et al. 2002), magnetic reconnection (He et al. 2009), or vortex shedding (Nakariakov et al. 2009). Recently, Nisticò et al. (2013) and Anfinogentov et al. (2013) detected low-amplitude (sub-megameter scale) kink oscillations of coronal loops. Kink waves in this category last for dozens of wave cycles without significant damping, and are apparently not associated with any explosive events (Anfinogentov et al. 2013). Transverse oscillatory motions were also observed in chromospheric spicules (Okamoto & De Pontieu 2011; Morton 2014), chromospheric mottles (Kuridze et al. 2012), filament threads (Lin et al. 2007, 2009), large prominences (Tripathi et al. 2009; Hershaw et al. 2011; Arregui et al. 2012), polar plumes (Thurgood et al. 2014), coronal rain (Antolin & Verwichte 2011), helmet streamers (Chen et al. 2010, 2011), and even coronal mass ejections (Lee et al. 2015).

Fundamental (global) standing kink modes are frequently observed in closed coronal loops (Ruderman & Erdélyi 2009; Van Doorsselaere et al. 2009). The period of coronal transverse waves ranges from 2 to 33 minutes; and the damping time has a similar timescale (Aschwanden et al. 2002; White & Verwichte 2012). The curved coronal loops are normally assumed to be approximately co-planar; the loop plane intrinsically defines horizontally and vertically polarized kink waves about the loop axis (Ruderman 2009). Horizontal kink waves are more frequently observed, e.g., Nakariakov et al. (1999), Schrijver et al. (2002), Aschwanden et al. (2002), and Zimovets & Nakariakov (2015), while vertical kink waves were only reported in a limited number of cases, e.g., Wang & Solanki (2004), Verwichte et al. (2006), Selwa et al. (2007, 2010, 2011), White et al. (2012), and Kim et al. (2014).

The main interest in standing kink modes of coronal loops mainly arises from their role in diagnosing the coronal plasma via MHD seismology (Nakariakov & Verwichte 2005; De

Moortel & Nakariakov 2012). The standing kink mode could be used as a tool to infer magnetic field strength along a coronal loop (Nakariakov & Ofman 2001; Verwichte et al. 2009, 2010, 2013a). Verwichte et al. (2013b) measured the range of the density contrast and inhomogeneity layer thickness of coronal loops based on the period-damping timescaling law. De Moortel & Pascoe (2009) are the first to validate MHD seismology with three-dimensional (3D) numerical simulations, and showed that the inverted magnetic field strength agrees with the input magnetic field within a factor of about two. Aschwanden & Schrijver (2011) and Verwichte et al. (2013a) compared the seismological field and the Alfvén-transit-time-averaged value in the potential field model, and found consistency within an order of magnitude. Chen & Peter (2015) performed MHD simulations using a realistic coronal model and found that the excited coronal loop oscillations would be effectively used to infer the average magnetic field.

Kink MHD waves are highly incompressible in the long wavelength limit and exhibit only quasi-rigid motions (Goossens et al. 2012). Indeed, in a coronal loop the density (or temperature) perturbation by a kink mode is at the order of 10^{-3} or less than the equilibrium value. The observed intensity variations of coronal loops (e.g., O'Shea et al. 2007; Verwichte et al. 2009, 2010) are ascribed to the column depth modulation introduced by the kink motion. Cooper et al. (2003a, 2003b) performed line of sight (LOS) integration through the coronal loop plasma perturbed by MHD waves and demonstrated that intensity modulation could become significant in case of a kink mode, even though the plasma fluid compression is negligible.

Recently, Goossens et al. (2014) showed that the kink mode solution could be decomposed into a quasi-rigid transverse motion and a rotational motion, which is detectable as Doppler velocity oscillations in optically thick lines. That paper confronts interpreting rotational motion as a signature of Alfvén wave (De Pontieu et al. 2012). Therefore, forward modeling would significantly advance the knowledge of kink modes and resolve the dispute on whether a wave with observed rotational motion is a kink or Alfvén wave (e.g., Van Doorsselaere et al. 2008). Moreover, MHD seismology and wave energy estimation strongly rely on correct identification of the wave mode and accurate measurements of wave properties (Goossens et al. 2012; Van Doorsselaere et al. 2014).

Forward modeling is a novel approach that synthesizes the plasma emission observables (Antolin & Van Doorsselaere 2013; Yuan et al. 2015b). It basically converts analytical or numerical models into observables. Therefore, the inversion process (e.g., MHD seismology, MHD spectroscopy, helioseismology, X-ray tomography), which is originally ill-posed due to the lack of sufficient constraints (or observables), could be better understood in the sense that knowledge of plasma properties is given a priori. Gruszecki et al. (2012) studied the geometric integration of the plasma density of a fast sausage mode of a plasma cylinder. De Moortel & Bradshaw (2008) demonstrated that the damping rate measured in EUV emission intensity oscillations may not reflect the real damping of MHD waves. Antolin & Van Doorsselaere (2013) and Antolin et al. (2014) considered the inhomogeneous plasma emission introduced by fast sausage modes and found that the LOS effect and spatial resolution would significantly modify the associated EUV emissions of coronal loops. Yuan et al. (2015b) found that the contribution function of atomic emission (Dere et al. 1997) could cause emission asymmetry for positive and negative temperature perturbations, and could even lead to the detection of half-periodicity.

In this study, we present a forward modeling study of the standing kink modes of coronal loops. Section 2 gives the analytical solution of a kink mode in a coronal loop and the numerical discretization for the forward modeling code.[4] Section 3 and Section 4 present our results and conclusions, respectively.

2. MODEL

2.1. Standing Kink Mode

In this paper, we study the standing kink wave in a plasma cylinder embedded in a uniform plasma. The magnetic field is parallel to the axis of the plasma cylinder (i.e., z-axis), $\boldsymbol{B}_0 = B_0 \hat{\boldsymbol{z}}$. The equilibrium magnetic field B_0, plasma density ρ_0, and temperature T_0 are piecewise functions of the r-coordinate:

$$B_0, \rho_0, T_0 = \begin{cases} B_{\mathrm{i}}, \rho_{\mathrm{i}}, T_{\mathrm{i}}, & \text{for } r \leqslant a \\ B_{\mathrm{e}}, \rho_{\mathrm{e}}, T_{\mathrm{e}}, & \text{for } r > a, \end{cases} \quad (1)$$

where a is the radius of the loop. Hereafter, we use the subscripts "i" and "e" to differentiate the internal and external equilibrium values of the loop system.

The linearized ideal MHD equations give the perturbed quantities that deviate from the magnetostatic equilibrium (see, e.g., Ruderman & Erdélyi 2009):

$$\rho_1 = -\nabla \cdot (\rho_0 \boldsymbol{\xi}), \quad (2)$$

$$\rho_0 \frac{\partial^2 \boldsymbol{\xi}}{\partial t^2} = -\nabla P_{\mathrm{T1}} + \frac{1}{\mu_0}[(\boldsymbol{B}_0 \cdot \nabla)\boldsymbol{b}_1 + (\boldsymbol{b}_1 \cdot \nabla)\boldsymbol{B}_0], \quad (3)$$

$$\boldsymbol{b}_1 = \nabla \times (\boldsymbol{\xi} \times \boldsymbol{B}_0), \quad (4)$$

$$p_1 - C_{\mathrm{s}}^2 \rho_1 = \boldsymbol{\xi} \cdot (C_{\mathrm{s}}^2 \nabla \rho_0 - \nabla p_0), \quad (5)$$

where $\boldsymbol{\xi}$ is the Lagrangian displacement vector, ρ_0, p_0, and $\boldsymbol{B}_0$ are the plasma density, pressure, and magnetic field in equilibrium, ρ_1, p_1 and $\boldsymbol{b}_1$ are the perturbed plasma density, pressure and magnetic field, $P_{\mathrm{T1}} = p_1 + \boldsymbol{b}_1 \cdot \boldsymbol{B}_0/\mu_0$ is the perturbed total pressure, and μ_0 is the magnetic permeability in free space. A few typical speeds are defined to describe the loop system: $C_{\mathrm{s}} = \sqrt{\gamma p_0/\rho_0}$, $C_{\mathrm{A}} = B_0/\sqrt{\mu_0 \rho_0}$, and $C_{\mathrm{T}} = C_{\mathrm{A}} C_{\mathrm{s}}/\sqrt{C_{\mathrm{A}}^2 + C_{\mathrm{s}}^2}$ are the acoustic, Alfvén, and tube speed, respectively (Edwin & Roberts 1983); and $\omega_{\mathrm{s}} = C_{\mathrm{s}}k$, $\omega_{\mathrm{A}} = C_{\mathrm{A}}k$, and $\omega_{\mathrm{T}} = C_{\mathrm{T}}k$ are the corresponding acoustic, Alfvén, and tube frequencies, where $k = \pi n/L_0$ is the longitudinal wavenumber, n is the longitudinal mode number ($n = 1$ corresponds to the fundamental mode), L_0 is the length of the loop, and $\gamma = 5/3$ is the adiabatic index.

The boundary value problem (Equation (2)–(5)) is solved in cylindrical coordinates (r, ϕ, z) with the Neumann boundary conditions at $r = a$,

$$[P_{\mathrm{T}}]_{r=a} = 0, \quad (6)$$

$$[\xi_r]_{r=a} = 0, \quad (7)$$

and the Dirichlet boundary conditions at $r = 0, \infty$

$$P_{\mathrm{T}}|_{r=0} < \infty, \quad (8)$$

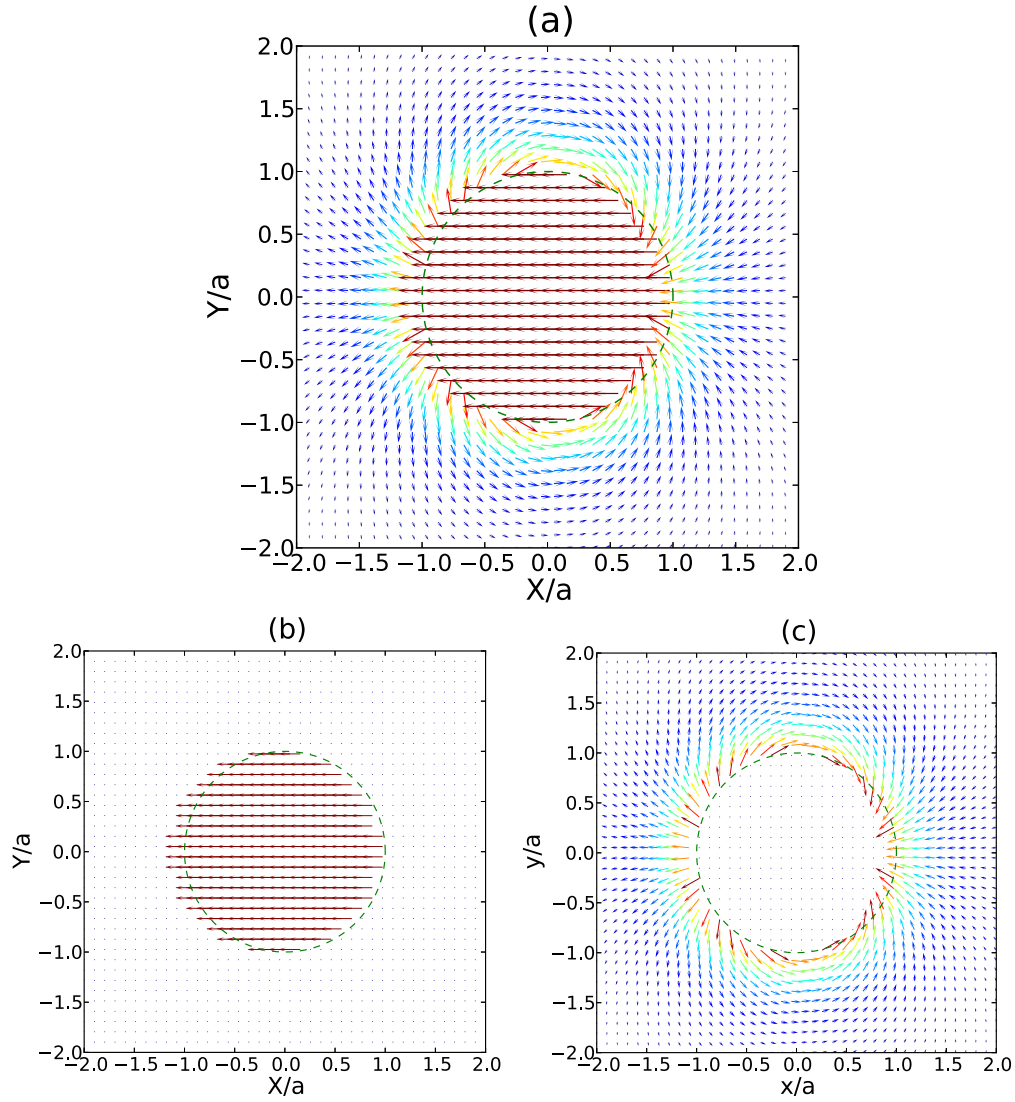[4] The FoMo code is available at https://github.com/TomVeeDee/FoMo

Figure 1. Flow fields at the cross-section of $z = L_0/2$. (a) illustrates the full solution $[\tilde{v}_x, \tilde{v}_y]^T$, whereas (b) and (c) show the polarized quasi-rigid motion $[\tilde{v}_x^{[1]}, \tilde{v}_y^{[1]}]^T$ and the quadrupole term $[\tilde{v}_x^{[2]}, \tilde{v}_y^{[2]}]^T$.

$$\xi^2|_{r=0} < \infty, \qquad (9)$$

$$P_T|_{r\to\infty} = 0, \qquad (10)$$

$$\xi^2|_{r\to\infty} = 0, \qquad (11)$$

where P_T and ξ_r are the total pressure and the radial displacement, respectively. In the case of the standing kink mode ($m = 1$), we Fourier-analyze the perturbed quantities by assuming $P_{T1} = A\mathcal{R}(r)\cos(\omega t)\sin(kz)\cos(\phi)$, where A is the amplitude of the perturbed total pressure. The longitudinal profile $\sin(kz)$ ensures that the transverse displacement follows a $\sin kz$-distribution, and therefore has a maximum at the loop apex for the fundamental mode ($n = 1$).

The perturbed total pressure P_{T1} (and $\mathcal{R}$) must satisfy

$$\frac{d^2 P_{T1}}{dr^2} + \frac{dP_{T1}}{r\,dr} - \left(\kappa_r^2 + \frac{1}{r^2}\right)P_{T1} = 0, \qquad (12)$$

where $\kappa_r^2 = \frac{(\omega_s^2 - \omega^2)(\omega_A^2 - \omega^2)}{(\omega_s^2 + \omega_A^2)(\omega_T^2 - \omega^2)}k^2$ is the square of the radial wavenumber and has the dimensionality of wavenumber k^2. Equation (12) holds for both internal and external plasma,

where all quantities are piecewise functions of r, and gives $\mathcal{R} = J_1(|\kappa_{ri}|r)$ or $K_1(\kappa_{re}r)$ for $r < a$ and $r > a$, respectively, where J_1 and K_1 are the first order Bessel function of the first kind and the first order modified Bessel function of the second kind, respectively. We redefine $|\kappa_{ri}| = \sqrt{-\kappa_{ri}^2}$, so the dispersion relation for the fast body mode is obtained as

$$\frac{\kappa_{re}}{\rho_e(\omega_{Ae}^2 - \omega^2)}\frac{K_1'(\kappa_{re}a)}{K_1(\kappa_{re}a)} = \frac{|\kappa_{ri}|}{\rho_i(\omega_{Ai}^2 - \omega^2)}\frac{J_1'(|\kappa_{ri}|a)}{J_1(|\kappa_{ri}|a)}. \qquad (13)$$

The perturbed Lagrangian quantities used in the forward modeling code are:

$$v_r = \hat{v}_r(r)\sin(\omega t)\sin(kz)\cos\phi, \qquad (14)$$

$$v_\phi = \hat{v}_\phi(r)\sin(\omega t)\sin(kz)\sin\phi, \qquad (15)$$

$$v_z = \hat{v}_z(r)\sin(\omega t)\cos(kz)\cos\phi, \qquad (16)$$

$$\rho_1 = \hat{\rho}_1(r)\cos(\omega t)\sin(kz)\cos\phi, \qquad (17)$$

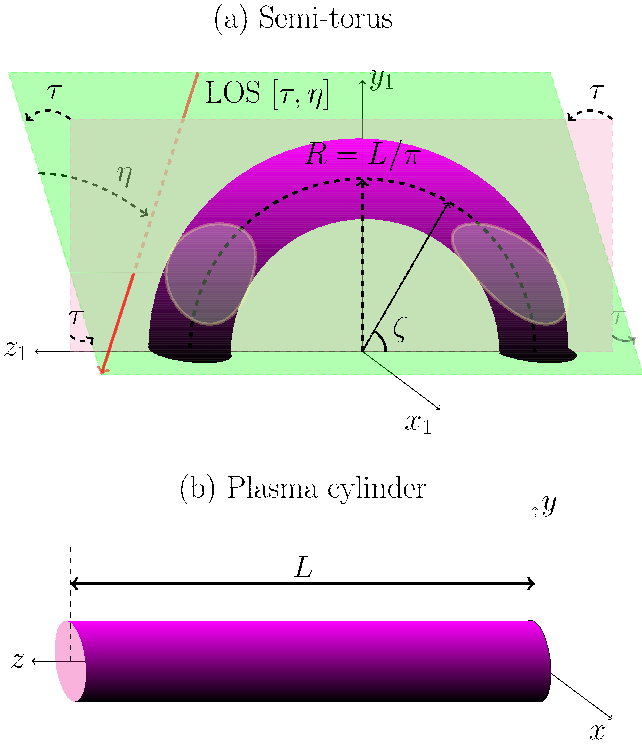$$T_1 = \hat{T}_1(r)\cos(\omega t)\sin(kz)\cos\phi, \qquad (18)$$

(a) Semi-torus

(b) Plasma cylinder

Figure 2. Schematic drawing illustrating how the cylinder is mapped into a semi-torus and the LOS angle definition. The pink plane ($y_1 z_1$ plane) is defined by the loop spine. The green plane forms an angle of τ with the pink plane and their line of intersection is parallel with the z_1-axis. The LOS is free to vary within the green plane and is quantified by an angle $\eta + \pi/2$ relative to the z_1-axis or the line of intersection. An LOS angle is denoted as $[\tau, \eta]$.
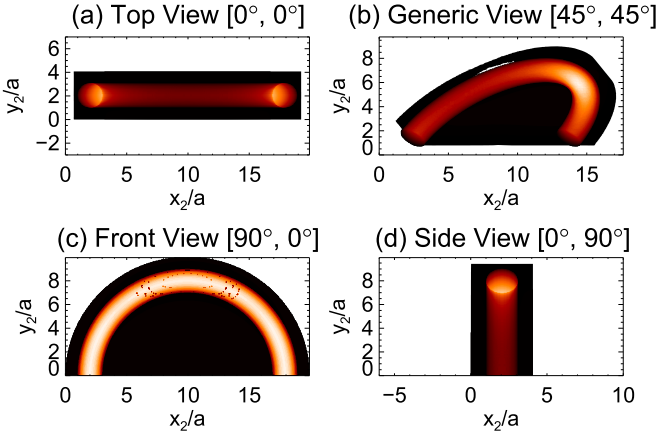
(a) Top View [0°, 0°]   (b) Generic View [45°, 45°]

(c) Front View [90°, 0°]   (d) Side View [0°, 90°]

Figure 3. Fe IX $\lambda 171.073$ Å synthetic emission at (a) the top view, (b) the generic view, (c) the front view, and (d) the side view. The origins and ranges of the plots are chosen to best match the relative geometries at various views, and will not affect the results at all.

(An animation of this figure is available.)

where

$$\hat{v}_r = -\frac{r d\mathcal{R}}{\mathcal{R} dr}\hat{v}_0(r), \tag{19}$$

$$\hat{v}_\phi = \hat{v}_0(r) = \frac{A\mathcal{R}\omega}{r\rho_0(\omega^2 - \omega_A^2)}, \tag{20}$$

$$\hat{v}_z = -\frac{C_T^2 kr}{C_A^2}\frac{(\omega^2 - \omega_A^2)}{(\omega^2 - \omega_T^2)}\hat{v}_0, \tag{21}$$

$$\hat{\rho}_1 = \frac{(\omega^2 - \omega_A^2)}{(\omega^2 - \omega_T^2)}\frac{\rho_0 r\omega\hat{v}_0}{(C_s^2 + C_A^2)}, \tag{22}$$

$$\hat{T}_1 = \frac{(\omega^2 - \omega_A^2)}{(\omega^2 - \omega_T^2)}\frac{(\gamma - 1)T_0 r\omega\hat{v}_0}{(C_s^2 + C_A^2)}. \tag{23}$$

The horizontally polarized kink mode has

$$v_x = \tilde{v}_x(r, \phi)\sin(\omega t)\sin(kz), \tag{24}$$

$$v_y = \tilde{v}_y(r, \phi)\sin(\omega t)\sin(kz), \tag{25}$$

where

$$\tilde{v}_x = \hat{v}_r\cos^2\phi - \hat{v}_\phi\sin^2\phi \tag{26}$$

$$= \begin{cases} v_{00}(J_0 - J_2\cos 2\phi), & \text{for } r \leqslant a \\ -\dfrac{J_1'(|\kappa_{ri}|a)}{K_1'(\kappa_{re}a)}v_{00}(K_0 + K_2\cos 2\phi), & \text{for } r > a, \end{cases} \tag{27}$$

$$\tilde{v}_y = \hat{v}_r\cos\phi\sin\phi + \hat{v}_\phi\cos\phi\sin\phi \tag{28}$$

$$= \begin{cases} -v_{00}J_2\sin 2\phi, & \text{for } r \leqslant a \\ -\dfrac{J_1'(|\kappa_{ri}|a)}{K_1'(\kappa_{re}a)}v_{00}K_2\sin 2\phi, & \text{for } r > a, \end{cases} \tag{29}$$

and $v_{00} = -\dfrac{A_i\omega|\kappa_{ri}|}{2\rho_i(\omega^2 - \omega_{Ai}^2)}$ is the Lagrangian velocity at $r = 0$.

We could see that the plasma motion is predominantly polarized along the x-direction described by the J_0 term (also see the Appendix and Goossens et al. 2014). The quadrupole terms $J_2\cos(2\phi)$ and $J_2\sin(2\phi)$ may contribute to the fine structuring of coronal loops associated with kink modes. The vertically polarized transverse mode could be easily obtained by replacing ϕ with $\phi + \pi/2$, while keeping the coordinate system intact.

We rewrite Equations (27) and (29) as

$$\begin{bmatrix} \tilde{v}_x \\ \tilde{v}_y \end{bmatrix} = \begin{bmatrix} \tilde{v}_x^{[1]} \\ \tilde{v}_y^{[1]} \end{bmatrix} + \begin{bmatrix} \tilde{v}_x^{[2]} \\ \tilde{v}_y^{[2]} \end{bmatrix}, \tag{30}$$

$$\begin{bmatrix} \tilde{v}_x^{[1]} \\ \tilde{v}_y^{[1]} \end{bmatrix} = \begin{cases} v_{00}\begin{bmatrix} J_0 \\ 0 \end{bmatrix}, & \text{for } r \leqslant a, \\ -\dfrac{J_1'(|\kappa_{ri}|a)}{K_1'(\kappa_{re}a)}v_{00}\begin{bmatrix} K_0 \\ 0 \end{bmatrix}, & \text{for } r > a, \end{cases} \tag{31}$$

$$\begin{bmatrix} \tilde{v}_x^{[2]} \\ \tilde{v}_y^{[2]} \end{bmatrix} = \begin{cases} -v_{00}J_2\begin{bmatrix} \cos 2\phi \\ \sin 2\phi \end{bmatrix}, & \text{for } r \leqslant a \\ -\dfrac{J_1'(|\kappa_{ri}|a)}{K_1'(\kappa_{re}a)}v_{00}K_2\begin{bmatrix} \cos 2\phi \\ \sin 2\phi \end{bmatrix}, & \text{for } r > a. \end{cases} \tag{32}$$

In the thin flux tube limit ($ka \ll 1$), $J_0 = 1 + \mathcal{O}((ka)^2)$ for $r < a$, and $K_0/K_2 \ll 1$ for $r > a$, so the polarized quasi-rigid motion is almost confined within the tube $r < a$ (Figure 1(b)). The quadrupole term is of secondary effect, as $J_2 = \mathcal{O}((ka)^2)$ for $r < a$, whereas at $r > a$, $K_2/K_0 \gg 1$, so it dominates the surrounding plasma (Figure 1(c)). But we shall note that the quadrupole term is only a second order term inside the tube, whereas at the ambient plasma, its magnitude is of the first order.
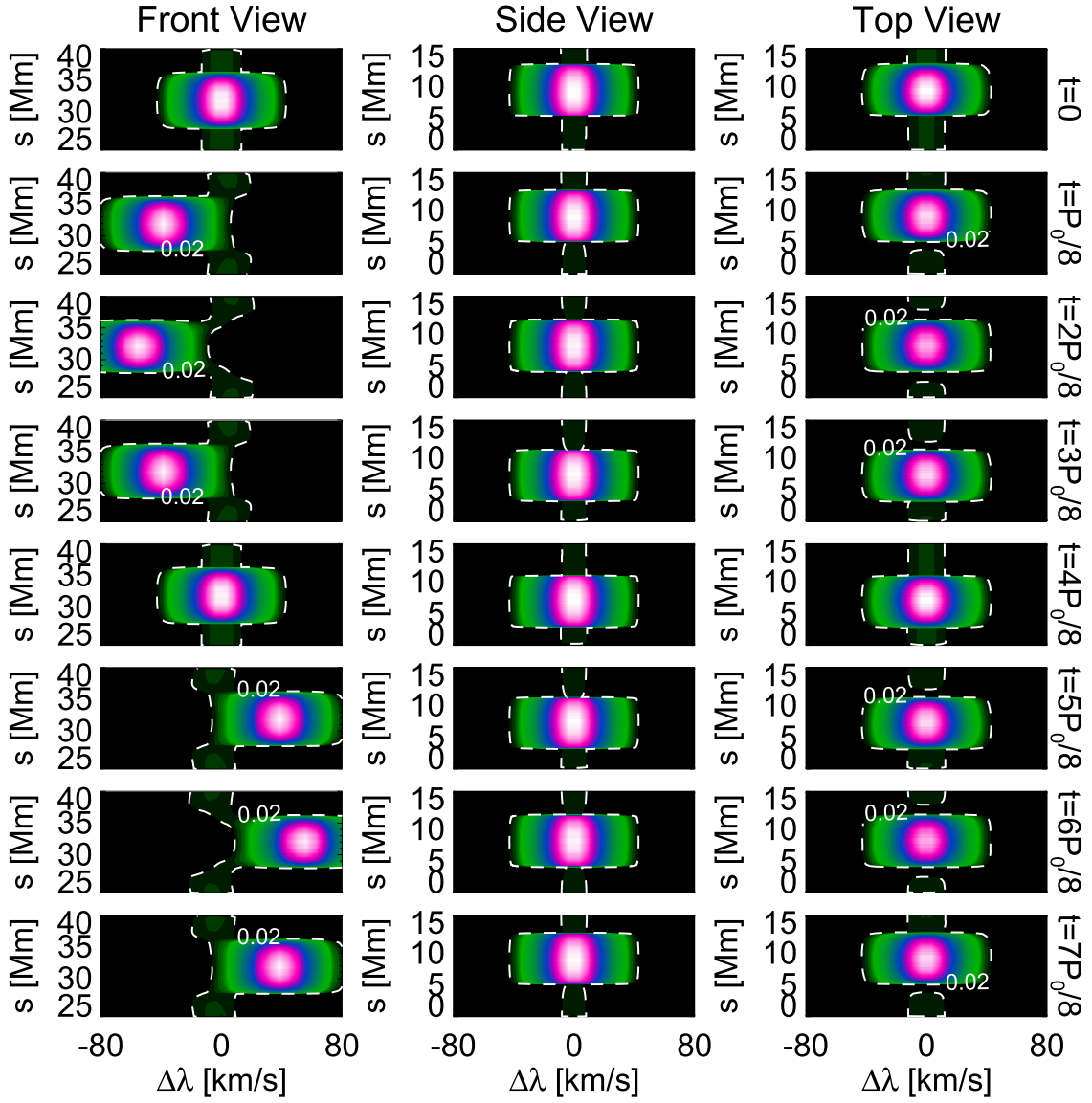
Figure 4. Fe IX λ171.073 Å spectra of sit-and-stare modes along slices *s* across the loop apex at the front view (left), the side view (middle), and the top view (right). The dashed lines contour the 0.02-level of the peak emission, and highlight the pendular motion at the front view.

(An animation of this figure is available.)

2.1.1. Correction for Advected Plasma Motion

Equations (14)–(18) are solutions in Lagrangian coordinates, while we need to synthesize observables at a fixed LOS (Eulerian coordinates), therefore the Lagrangian variables are remapped into Eulerian coordinates. The transverse displacement of a kink mode is of the order of the loop radius a (Aschwanden et al. 2002), and therefore, the advected motion cannot be neglected. The displacement $\boldsymbol{\xi}$ for the plasma fluid at the initial position $[r, \phi, z]$ could be obtained by integrating the velocity with respect to time t.

$$\xi_r = -\hat{v}_r/\omega \cos(\omega t)\sin(kz)\cos\phi, \qquad (33)$$

$$\xi_\phi = -\hat{v}_\phi/\omega \cos(\omega t)\sin(kz)\sin\phi, \qquad (34)$$

$$\xi_z = -\hat{v}_z/\omega \cos(\omega t)\cos(kz)\cos\phi. \qquad (35)$$

In Cartesian coordinates, the displacement is given as

$$\xi_x = \tilde{\xi}_x \cos(\omega t)\sin(kz), \qquad (36)$$

$$\xi_y = \tilde{\xi}_y \cos(\omega t)\sin(kz), \qquad (37)$$

where $[\tilde{\xi}_x, \tilde{\xi}_y]^{\mathrm{T}} = -[\tilde{v}_x, \tilde{v}_y]^{\mathrm{T}}/\omega$. Then the new position $[\tilde{x}, \tilde{y}, \tilde{z}]^{\mathrm{T}}$ of the plasma fluid originally at $[x, y, z]^{\mathrm{T}} = [r\cos\phi, r\sin\phi, z]^{\mathrm{T}}$ is

$$\tilde{x}(t) = x + \xi_x(t), \qquad (38)$$

$$\tilde{y}(t) = y + \xi_y(t), \qquad (39)$$

$$\tilde{z}(t) = z + \xi_z(t). \qquad (40)$$

Thus, the plasma properties (e.g., $\rho_0 + \rho_1$) at location $[x, y, z]^{\mathrm{T}}$ will be moved to the position $[\tilde{x}, \tilde{y}, \tilde{z}]^{\mathrm{T}}$.
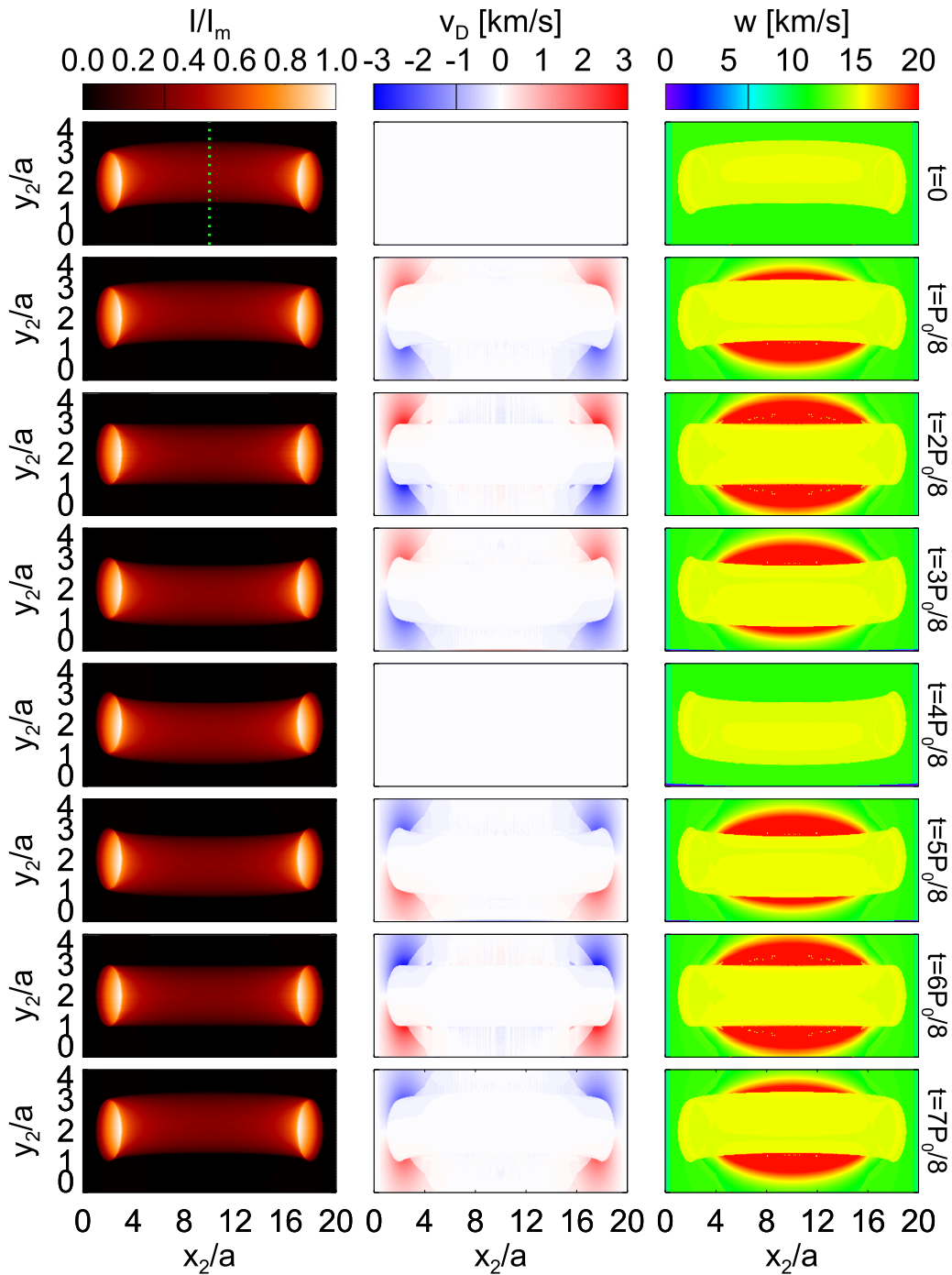
Figure 5. Snapshots of the relative emission I/I_m (left), Doppler shift velocity v_D (middle), and line width w (right).
(An animation of this figure is available.)

2.1.2. Mapping into a Semi-torus Structure

The loop curvature was found to have a secondary effect on the transverse motion of coronal loops (Van Doorsselaere et al. 2009), and therefore we only consider the LOS effect and plasma inhomogeneities by mapping the kink mode solution of a plasma cylinder into a semi-torus structure (see Figure 2). The kink mode displaces the axis of the loop, therefore it has a polarization relative to the plane defined by the static curved loop axis, i.e., the $y_1 z_1$ plane. It is defined as a horizontal kink mode if the loop oscillates out of the $y_1 z_1$ plane (e.g., Aschwanden et al. 1999; Nakariakov et al. 1999). Or otherwise, if the transverse motion of the loop axis is within the $y_1 z_1$ plane, it is termed as a vertical kink mode (e.g., Wang & Solanki 2004; Verwichte et al. 2006).

After correcting the advected motion, we map the plasma coordinates and the associated plasma parameters into a semi-torus structure (Figure 2). The plasma cylinder is bent into a torus within the $y_1 z_1$ plane using the following transform (also
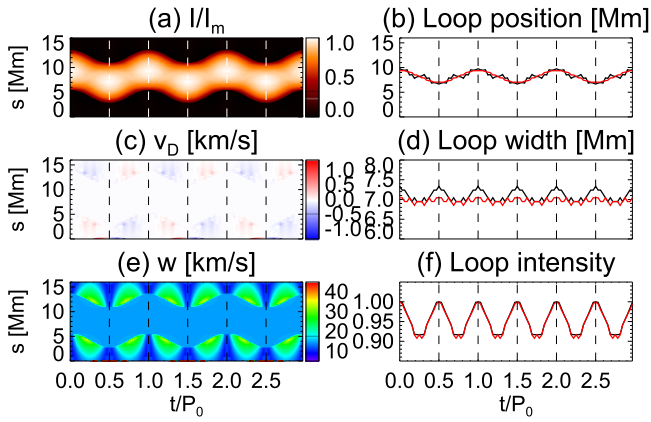
Figure 6. Sit-and-stare mode across the loop apex at the top view in the Fe IX λ171.073 Å line and the measurements of loop position, width, and intensity. The red continuous lines plot the corresponding case in the EIS resolution.

see Kuznetsov et al. 2015):

$$x_l = x, \tag{41}$$

$$y_l = (R + y)\sin \zeta, \tag{42}$$

$$z_l = -(R + y)\cos \zeta, \tag{43}$$

where $\zeta = z/R$, and $R = L/\pi$.

The velocity is transformed by

$$
\begin{bmatrix} v_{x_l} \\ v_{y_l} \\ v_{z_l} \end{bmatrix} =
\begin{bmatrix} 1 & 0 & 0 \\ 0 & \sin\zeta(z) & \cos\zeta(z) \\ 0 & -\cos\zeta(z) & \sin\zeta(z) \end{bmatrix}
\begin{bmatrix} v_x \\ v_y \\ v_z \end{bmatrix}. \tag{44}
$$

This is basically a rotation of the velocity vector by an angle of $\zeta - \pi/2$ about the x-axis; and $\zeta - \pi/2$ varies within $[-\pi/2, \pi/2]$ for $z \in [0, L]$.

2.2. Coronal Loop Model

Coronal loops are highly complex and dynamic structures, observed within a broad range of plasma conditions; see a review by Reale (2014). The loop width varies from a few hundreds (Brooks et al. 2013; Morton & McLaughlin 2013) to thousands of kilometers (Aschwanden et al. 2002; Aschwanden & Nightingale 2005; Aschwanden & Schrijver 2011). A coronal loop may have multi-thermal (Nisticò et al. 2014a), multi-stranded structures (Peter et al. 2013; Scullion et al. 2014), and may be associated with heating and flows (Winebarger et al. 2002; Klimchuk 2006; Hood et al. 2009). In our study, these fine structures are not considered; and the gravitational stratification is also neglected. Numerical simulations are required to model these features of coronal loop oscillations.

A coronal loop is set up in an equilibrium state. The loop measures $L_0 = 100$ Mm in length and $a = 4$ Mm in radius. The loop density and temperature are $\rho_i = 2.5 \cdot 10^{-12}$ kg m^{-3} ($n_{ei} = 1.5 \cdot 10^9$ cm^{-3}) and $T_i = 0.8$ MK, respectively. The internal plasma is permeated by a uniform magnetic field $B_i = 15$ G. We choose a density and temperature ratio of $\rho_i/\rho_e = 5$ and $T_i/T_e = 1.5$, respectively, then the magnetic field strength ratio is obtained by balancing the total pressure at the loop boundary. The plasma beta gives $\beta_i = 0.037$ and $\beta_e = 0.0048$ for the internal and external plasma, respectively. The corresponding acoustic speeds are $C_{si} = 150$ km s^{-1} and $C_{se} = 120$ km s^{-1}, while the Alfvén speeds are

$C_{Ai} = 840$ km s^{-1} and $C_{Ae} = 1900$ km s^{-1}. These parameters are commonly observed in coronal loops (e.g., Aschwanden & Boerner 2011; Reale 2014).

For the fundamental mode ($n = 1$), the wavelength is much longer than the loop radius ($ka = 0.13$). The dispersion relationship (Equation (13)) finds a kink mode solution with a period at $P_0 = 3.0$ minute ($\omega = 0.034$). We choose $A_i = 0.15$ Pa, so that the velocity perturbation amplitude is about 55 km s^{-1}, and the amplitude of displacement about 1.6 Mm ($0.4a$). The kink mode could be considered as highly incompressible (Van Doorsselaere et al. 2008; Goossens et al. 2012); the density (temperature) perturbation is about 0.4% (0.3%) of the equilibrium value. These parameters are commonly observed by the TRACE and SDO/AIA instruments (Aschwanden et al. 2002; Aschwanden & Schrijver 2011).

2.3. Forward Model

The loop system was discretized as given by Equations (14)–(18) in Cartesian coordinates. We calculate the plasma properties in a domain of $x(y) \in [-2a, 2a]$ and $z \in [0, L_0]$ with $160 \times 160 \times 400$ grid cells. Forward modeling was performed with a fixed output mesh grid $N_{x_2} \times N_{y_2} = 170 \times 340$[5] (see details in Yuan et al. 2015b). In contrast to compressive MHD modes (Antolin & Van Doorsselaere 2013; Reznikova et al. 2014, 2015; Kuznetsov et al. 2015; Yuan et al. 2015b), the kink mode only perturbs the density and temperature to the order of 10^{-3}–10^{-4} of the equilibrium values; therefore the effect of the contribution function is of secondary order. The spatial distributions of the plasma properties play a key role in determining the observational features. So we only present the synthetic emission of the Fe IX λ171.073 Å line; however, the results should be applicable to other optically thin lines. The Fe XII λ193.509 Å line and the AIA 171 and 193 Å channel were also synthesized, but they only produce redundant results.

The LOS is defined with two independent angles $[\tau, \eta]$ (see illustration in Figure 2), where τ is the angle between the loop axis plane (pink plane or $y_l z_l$-plane) and another plane (green plane), which share a line of intersection parallel to the z_l-axis. The LOS forms an angle of $\eta + \pi/2$ relative to the z_l-axis (or the line of intersection). Hereafter, we refer to $[0°, 0°]$ as top view, $[0°, 90°]$ as side view, $[90°, 0°]$ as front view, and $[45°, 0°]$ as oblique view for reference. Figure 3 illustrates the synthetic views in the Fe IX λ171.073 Å line at selected viewing angles, while Figure 4 presents the spectra of the Fe IX λ171.073 Å line along a slice s perpendicular to the axis of the loop apex at each viewing angle, which is comparable with Figure 9 in Goossens et al. (2014). We note that the loop cross-sectional profile could by approximated by integrating the emissivity along a uniform media $2\sqrt{a^2 - r^2}$, thus giving a non-Gaussian profile. However, a Gaussian profile is normally assumed and practically observed, e.g., Verwichte et al. (2005), Aschwanden & Boerner (2011). It implies that coronal loops could be multi-thermal (e.g., Nisticò et al. 2014a), multi-stranded (Peter et al. 2013), or inhomogeneous (Van Doorsselaere et al. 2004). However, the point-spread function may also play a role, especially in low-resolution instruments. Inhomogeneity in a coronal loop is favored by the resonant absorption theory (Ruderman & Roberts 2002; Van Doorsselaere et al. 2004; Antolin et al. 2015; Okamoto et al. 2015),

---

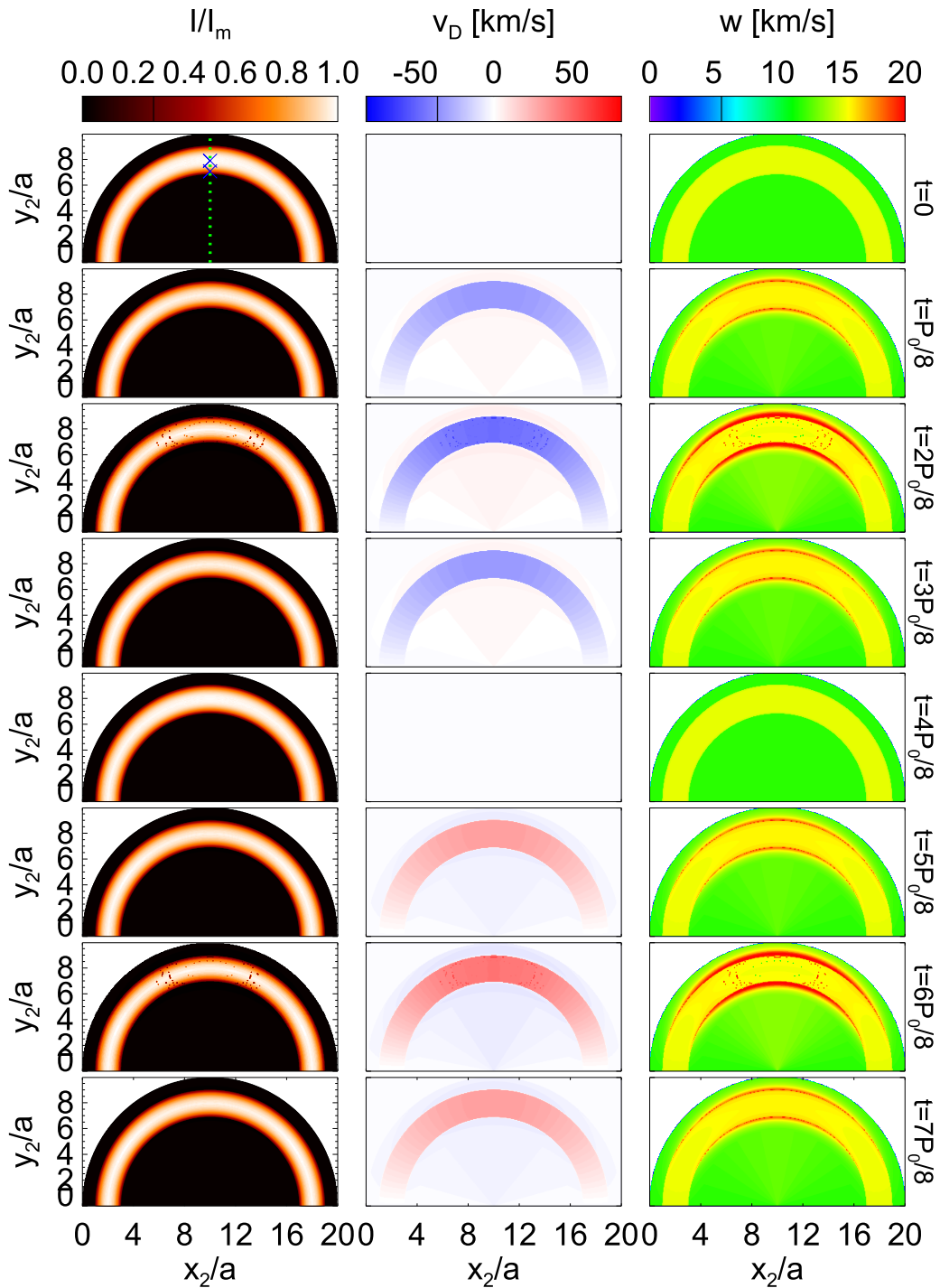[5] We refer to the projected output plane as the $x_2 y_2$ plane.

Figure 7. The same as Figure 5 but at the front view. Two crosses mark the positions at $r = 0$ and $r = 0.8a$ and the associated dynamic spectra are illustrated in Figure 13.

(An animation of this figure is available.)

which was developed to explain the strong damping of kink waves (Nakariakov et al. 1999). In this study, we do not consider the resonant absorption layer.

3. RESULTS

3.1. Top View

Figure 5 presents snapshots of the relative emission intensity I/I_m, Doppler shift velocity v_D, and line width w at the top

view, where I_m is the maximum intensity of the synthetic image series in each viewing angle. At the top view, the loop oscillates within the plane-of-sky; it is clearly seen in the relative intensity, Doppler shift velocity, and line width snapshots. The loop motion is not effectively observed in the Doppler shift, as the plasma motion inside and outside the loop is perpendicular to the LOS.

Figure 6 shows the sit-and-stare mode of a spectrograph, e.g., *Hinode*/EIS, in the Fe IX λ171.073 Å line. The time-
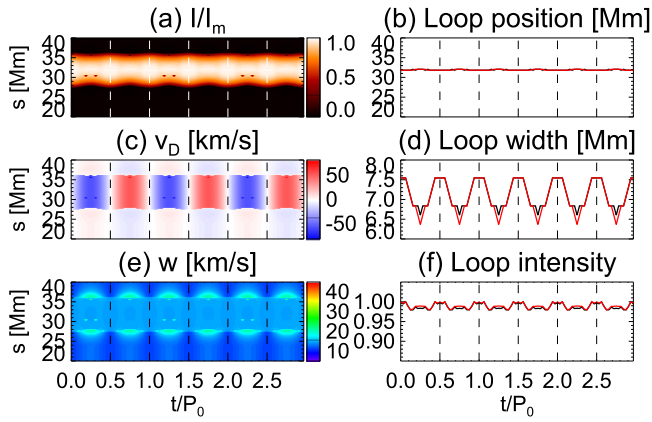
Figure 8. The same as Figure 6 but at the front view.

distance plot (see, e.g., Yuan & Nakariakov 2012) is taken at a cut perpendicular to the loop axis; see Figure 5. It clearly shows the transverse loop motion with an amplitude of about 1.5 Mm (0.4a); the associated intensity modulation is about 0.04. Intriguingly, we also detect loop width (Full-Width at Half-Maximum) variation between 7.0 Mm (1.7a) to 7.4 Mm (1.8a); the amplitude is about 0.2 Mm, one order of magnitude smaller than the loop displacement. The periodicity of the loop width and intensity variation is $P_0/2$. The Doppler shift velocity v_D is close to zero both inside and outside the loop. Moreover, one could also observe line broadening on the loop periphery. The line width variation has a period of $P_0/2$, and oscillates in phase with the loop intensity variation. Figure 4 (right column) illustrates this effect: the spectrum moves as a whole in space due to the transverse motion; however, the centroid of the spectrum remains unchanged, i.e., $v_D \simeq 0$ km s. At the loop periphery, one could observe significant periodic broadening. The background emission, about 2% of the loop emission, is associated with the quadrupole terms in Equations (27) and (29) (see the Appendix for derivations).

3.2. Front View

At the front view, the transverse motion is along the LOS, so the measured loop displacement is almost zero (Figure 7). The Doppler shift velocity and line width broadening at the loop edges are detectable. The time-distance plot (Figure 8) shows that the loop width oscillates with an amplitude of 0.1a and a period of $P_0/2$. The amplitude (about 0.1a) observed at the front view is about twice that (about 0.05a) measured at the top view. Again, we detect line width broadening at the periphery of the loop. This effect may contribute to the non-thermal broadening that has been observed at the edge of active region loops (Doschek et al. 2007). The associated Doppler shift (about 5 km s^{-1}) of the ambient plasma still exists (Figure 8); however, in contrast to the apparent rotational motion at the top view, the oscillation resembles a pendular motion relative to the loop oscillation. Figure 4 (left column) illustrates this effect: the Doppler shift on the periphery of the loop oscillates in anti-phase with the kink motion inside the loop, but with an amplitude of about 10% of the loop oscillation. This is consistent with Figure 9 in Goossens et al. (2014).

3.3. Oblique View

The oblique view (Figure 9) is the most frequently encountered observation on the solar disk. Figure 10 shows the time-distance plot observed in the Fe IX λ171.073 Å line. Loop oscillation features at the oblique view contain a mixture of the properties observed at the top and front views: loop displacement, intensity modulation, and loop width vary at moderate levels.

3.4. Side View

The side view and its variations are the most probable viewing angles for off-limb coronal loops; see, e.g., Verwichte et al. (2004). Figure 11 displays a complete cycle of the standing kink wave at the side view. Loop displacement is optimal for observation in the intensity, while the Doppler shift is very small. The line width does not exhibit significant spatial variation over the projected loop. However, line broadening is significantly measurable. The maximum line width broadening is not located at the loop apex; this is because at the apex the plasma motion is almost perpendicular, rather than along the LOS, and the projected fluid motion is only significant at some distance away from the apex.

Figure 12 presents the time-distance plot at the loop apex and the time series of the loop position, width, and intensity variations. The times series of the transverse motion is close to a sinusoidal profile, while in other viewing angles the loop displacement deviates significantly from a harmonic function. We note that at the side view, the loop width measures at $\simeq$8 Mm (about 2a), whereas other viewing angles normally do not reveal the full width of the loop. The associated loop width and intensity variations are very small.

4. DISCUSSION AND CONCLUSION

In this study, we discretized the fundamental standing kink wave solution of a plasma cylinder, corrected for the fluid advection, and mapped the solution into a semi-torus structure to simulate the kink MHD mode of a curved coronal loop. Then we synthesized the EUV emission in the Fe IX λ171.073 Å line and performed Gaussian fits to the spectra to obtain the observables, i.e., the emission intensity, Doppler shift velocity, and line width.

We find that the cross-sectional intensity distribution of a coronal loop filled with uniform plasma does not follow a Gaussian profile. This means that the complex coronal loop structure has to be considered to fully synthesize loop oscillations. More physics is associated with loop inhomo-geneities, i.e., resonant absorption (Ruderman & Roberts 2002; Van Doorsselaere et al. 2004), phase mixing (Heyvaerts & Priest 1983), and mode conversion (Pascoe et al. 2010, 2011, 2012).

Loop displacement could be observed in any viewing angle as long as the polarized motion is not along the LOS. This is the intrinsic feature of a kink MHD wave.

Since the density and temperature perturbations are of the order of 10^{-3}–10^{-4} of the equilibrium values, the contribution function has a negligible effect on the loop intensity modulation. The kink mode solution could be decomposed into a quasi-rigid transverse motion and a quadrupole term. The quadrupole term appears in both the v_x and v_y components of the transverse velocity (Equations (27) and (29)). The fluid elements at $[r, \phi]$ and $[r, -\phi]$ (or equally $[r, \phi]$ and $[r, \pi - \phi]$)
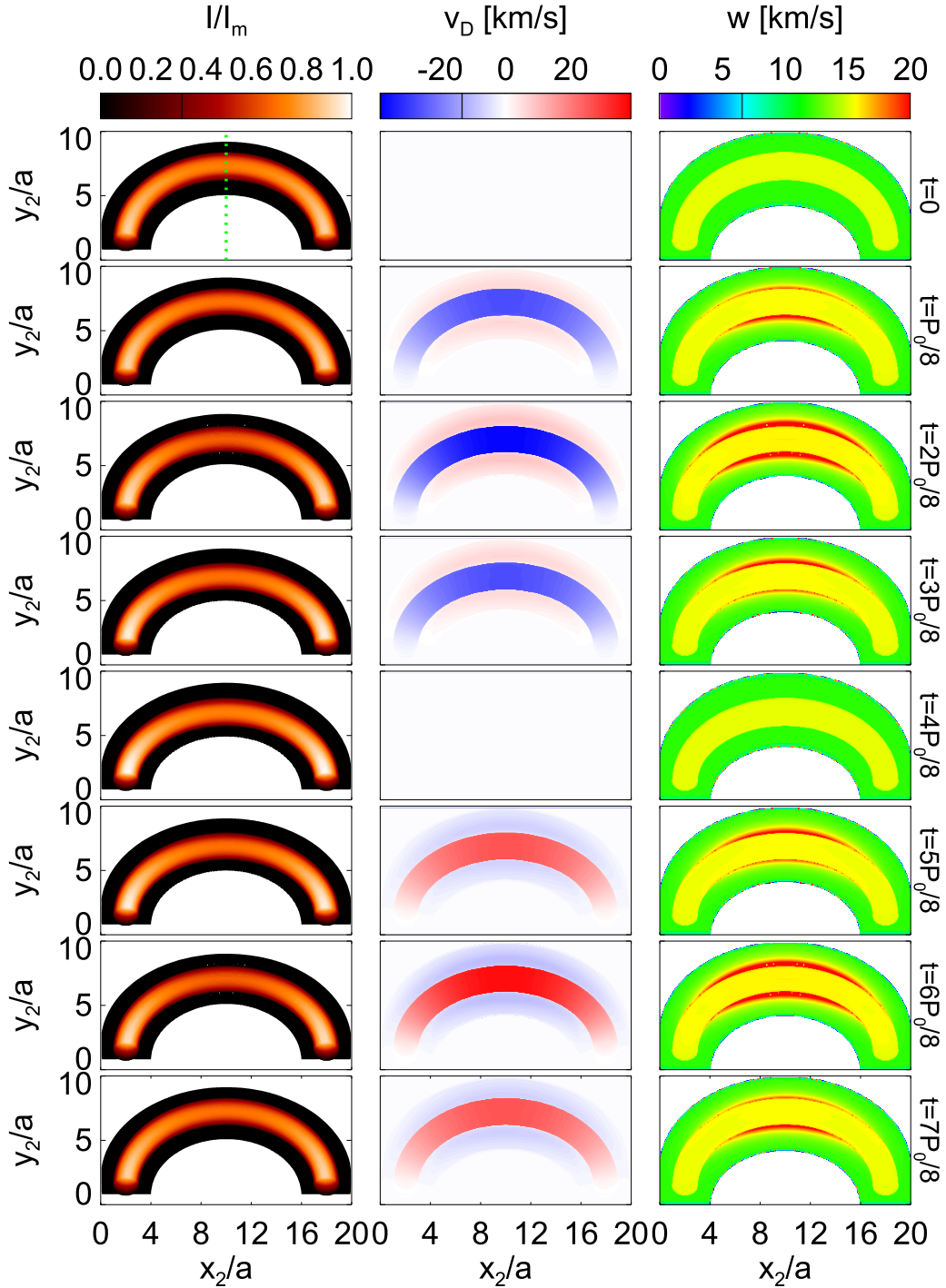
Figure 9. The same as Figure 5, but at the oblique view.
(An animation of this figure is available.)

outside the tube would periodically deform the r-shell in the Lagrangian coordinate at the order of $2\frac{J_1'(|\kappa_{ri}|a)}{K_1'(\kappa_{re}a)}v_{00}K_2/\omega$ (see Equations (31) and 32), which is a few percent of the loop radius a, if the amplitude of the displacement is close to a. Moreover, the fluid elements at $\pm\phi$ of the r-shell move to the opposite direction (Figure 14), and thus cause spectral line broadening. The broadening is also accompanied by intensity suppression, as illustrated in Figure 13. At the front view, the emission suppression at $r = 0.8a$ is stronger than that at the

loop axis. The quadrupole term effect only becomes significant at the loop edges, where the LOS integrates through more ambient plasma, and has a smaller impact on the spectrum at the loop axis, as the major contributions are from the plasma inside the tube.

Line width broadening is usually measured in the periphery of the loop, where ambient plasma emission is significant. It is associated with the $\cos(2\theta)$ and $\sin(2\theta)$ terms in Equations (27) and (29). The line broadening is observed at all views.
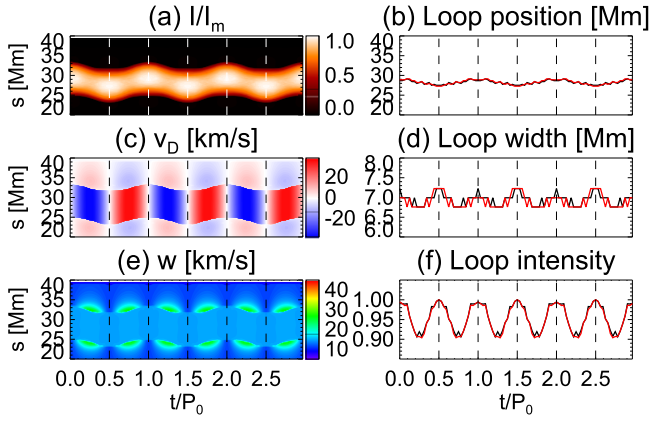
Figure 10. The same as Figure 6 but at the oblique view.

Figure 14 illustrates the reason: at the front view v_x could vary from positive to negative along a LOS at loop edge, whereas at the top view v_y is anti-symmetric about the xz-plane. This is consistent with the case of a vertical transverse wave (Van Doorsselaere & Nakariakov 2008). Doschek et al. (2007) reported non-thermal broadening at the edge of active region loops, and it may be connected with kink mode perturbations in the loops. However, since there is no report of the associated transverse motion, it may imply that coronal loops have unresolved low-amplitude motions similar to those found by Nisticò et al. (2013) and Anfinogentov et al. (2013).

The intensity modulation at the loop axis is usually detectable. This differs from the findings of Cooper et al. (2003a, 2003b), who only considered static plasma emission. In our study, the spectrum modifications by the MHD wave motions are considered and measured as if they are occurring in realistic observations. This factor could contribute to the integrated LOS intensity variation at the loop axis.

At the front view and its variations, a pendular motion is observed. At the front view, the transverse motion of the loop could be fully observed along the LOS, while the background emission oscillates at an amplitude of a few percent of the loop oscillation amplitude.

It is intriguing that the coronal loop is observed to have an apparent periodic expansion and contraction when undergoing a kink MHD mode wave. The optimal viewing angle to observe this effect is the front view. The amplitude of the loop width variation is about 20%–30% of the transverse loop motion. At the top view, the loop width variation is about half of the amplitude measured at the front view. At the side view, this effect could not be observed. The loop deformation introduced by the quadrupole terms alone is not fully responsible for the loop width variation at such an amplitude. The line width broadening would result in emission intensity suppression at the loop edges, and therefore the effective width of the loop measured in the emission intensity profile is smaller. In such a scenario, we detect effective loop width modulation associated with the periodic redistribution of the intensity across the loop. Aschwanden & Schrijver (2011) reported loop cross-sectional variations in a vertically polarized standing kink mode and interpreted it as a signature of coupled kink and sausage modes. In our simulation, we predict that the loop width oscillates at a similar amplitude, but with half the period of the kink mode. According to our modeling, Aschwanden & Schrijver (2011) may have observed an overlap of a steady loop and an

oscillating loop of similar density and temperature distribution. Therefore, the loop width variation could be accurately measured. The second paper (Yuan & Van Doorsselaere 2016) in this series will present the modeling details of this event.

In our loop system, the plasma emission of the coronal loop is about two orders of magnitude larger than the background. If the background emission becomes comparable to that of the loop, the spectroscopic measurement is still valid to some extent (Yuan et al. 2015b). However, one may opt to use another spectral line that is much more sensitive to the plasma emission of interest.

The resolutions of the forward models in each view are better than those offered by current instruments, i.e., *Hinode*/EIS. Therefore, to predict the possible observations with EIS, we degrade the resolution to an EIS level (1″) by averaging with the neighboring pixel. The red time series in Figures 6, 8, 10, and 12 represent the possible sit-and-stare observations with EIS. The loop width is generally measured to be smaller with low-resolution instruments, while the other parameters appear to be a smoothed version of those measured with high-resolution instruments, e.g., the SPICE instrument on board the *Solar Orbiter*.

In this study, we only consider the specific case of a standing kink wave in a coronal loop and synthesize the Fe IX λ171.073 Å emissions. However, it should be generally applicable to other optically thin emission lines because in the kink MHD mode, the perturbations to the density and temperature are very tiny. Therefore the spatial distribution of the velocity field plays a determining role in the observational signatures.

APPENDIX
DERIVATION OF THE QUADRUPOLE TERMS

Here we demonstrate the derivation of Equations (27) and (29).

$$\tilde{v}_x = \hat{v}_r \cos^2 \phi - \hat{v}_\phi \sin^2 \phi, \tag{45}$$

$$= \frac{-A\omega\kappa_r}{\rho_0(\omega^2 - \omega_A^2)}\left(\frac{d\mathcal{R}}{\kappa_r dr}\cos^2 \phi + \frac{\mathcal{R}}{\kappa_r r}\sin^2 \phi\right). \tag{46}$$

We define $\lambda = \kappa_r r$ and $\mathcal{R}'(\lambda) = d\mathcal{R}/d\lambda$. For the plasma motion inside the loop $r < a$:

$$\frac{d\mathcal{R}}{\kappa_r dr}\cos \phi^2 + \frac{\mathcal{R}}{\kappa_r r}\sin \phi^2 = J_1'(\lambda)\cos^2 \phi + \frac{J_1(\lambda)}{\lambda}\sin^2 \phi \tag{47}$$

$$= \left(\frac{J_1}{\lambda} - J_2\right)\cos^2 \phi + \frac{J_1(\lambda)}{\lambda}\sin^2 \phi \tag{48}$$

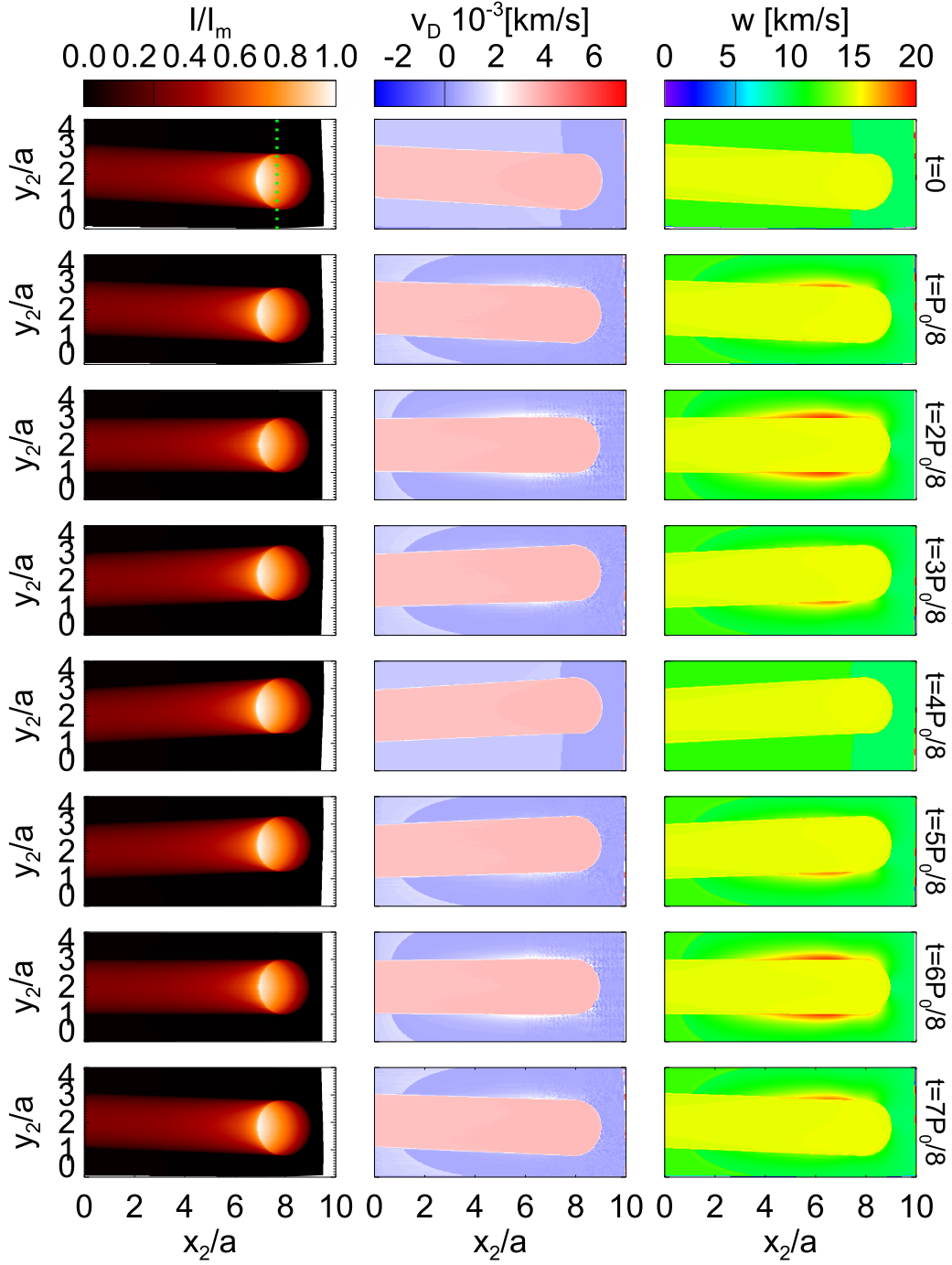$$= \frac{J_1}{\lambda} - J_2 \cos^2 \phi \tag{49}$$

Figure 11. The same as Figure 5 but at the side view.
(An animation of this figure is available.)

$$= \frac{J_1}{\lambda} - \frac{J_2}{2} - \frac{J_2}{2}\cos 2\phi \qquad (50)$$

$$= \frac{J_0 - J_2\cos 2\phi}{2}, \qquad (51)$$

where we used $J_1'(\lambda) = J_1/\lambda - J_2$ and $J_2 = 2J_1/\lambda - J_0$ (Olver et al. 2010) in the derivation. We followed the same procedure and used $K_1' = K_1/\lambda - K_2$ and $K_2 = 2K_1/\lambda + K_0$ (Olver et al. 2010). Then we obtained the plasma motion outside the

loop $r > a$:

$$\frac{d\mathcal{R}}{\kappa_r dr}\cos\phi^2 + \frac{\mathcal{R}}{\kappa_r r}\sin\phi^2 = K_1'(\lambda)\cos^2\phi + \frac{K_1(\lambda)}{\lambda}\sin^2\phi \qquad (52)$$

$$= \frac{K_1}{\lambda} - K_2\cos^2\phi \qquad (53)$$
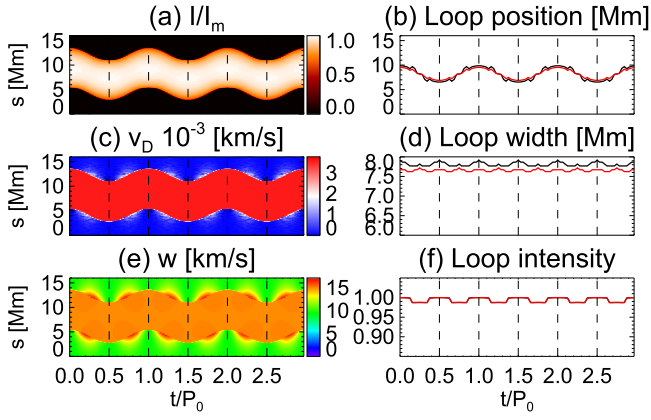
$$= -\frac{K_0 + K_2\cos 2\phi}{2}. \qquad (54)$$

Figure 12. The same as Figure 6 but at the side view.

Figure 13. Dynamic spectra extracted at positions $r = 0$ (a) and $r = 0.8a$ (b) at the front view, as labeled in Figure 7.

Here, we obtain the horizontal motion,

$$
\tilde{v}_x = \begin{cases} \dfrac{-A_i \omega |\kappa_{ri}|}{2\rho_i (\omega^2 - \omega_{Ai}^2)}(J_0 - J_2 \cos 2\phi), & \text{for } r \leqslant a \\[4mm] \dfrac{-A_e \omega \kappa_{re}}{2\rho_e (\omega^2 - \omega_{Ae}^2)}(-K_0 - K_2 \cos 2\phi), & \text{for } r > a. \end{cases}
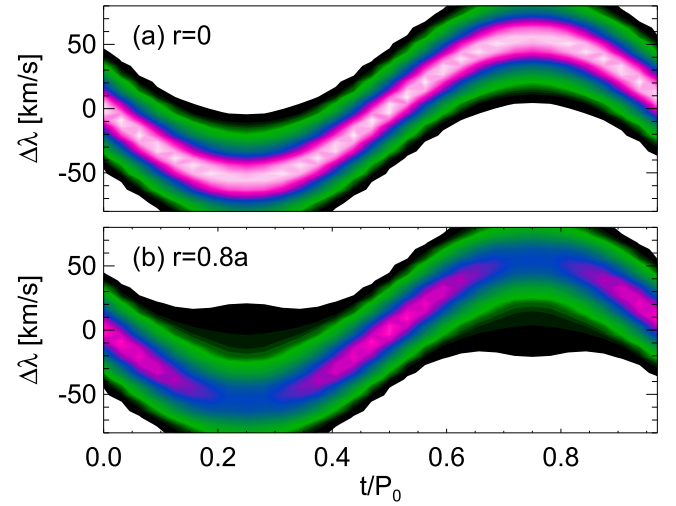\tag{55}
$$

At $r = 0$, $\tilde{v}_x = v_{00} = \dfrac{-A_i \omega |\kappa_{ri}|}{2\rho_i (\omega^2 - \omega_{Ai}^2)}$; while at $r = a$ and $\phi = 0$ or π,

$$
\tilde{v}_x|_{r=a^-} = v_{00}(J_0(|\kappa_{ri}|a) - J_2(|\kappa_{ri}|a)),
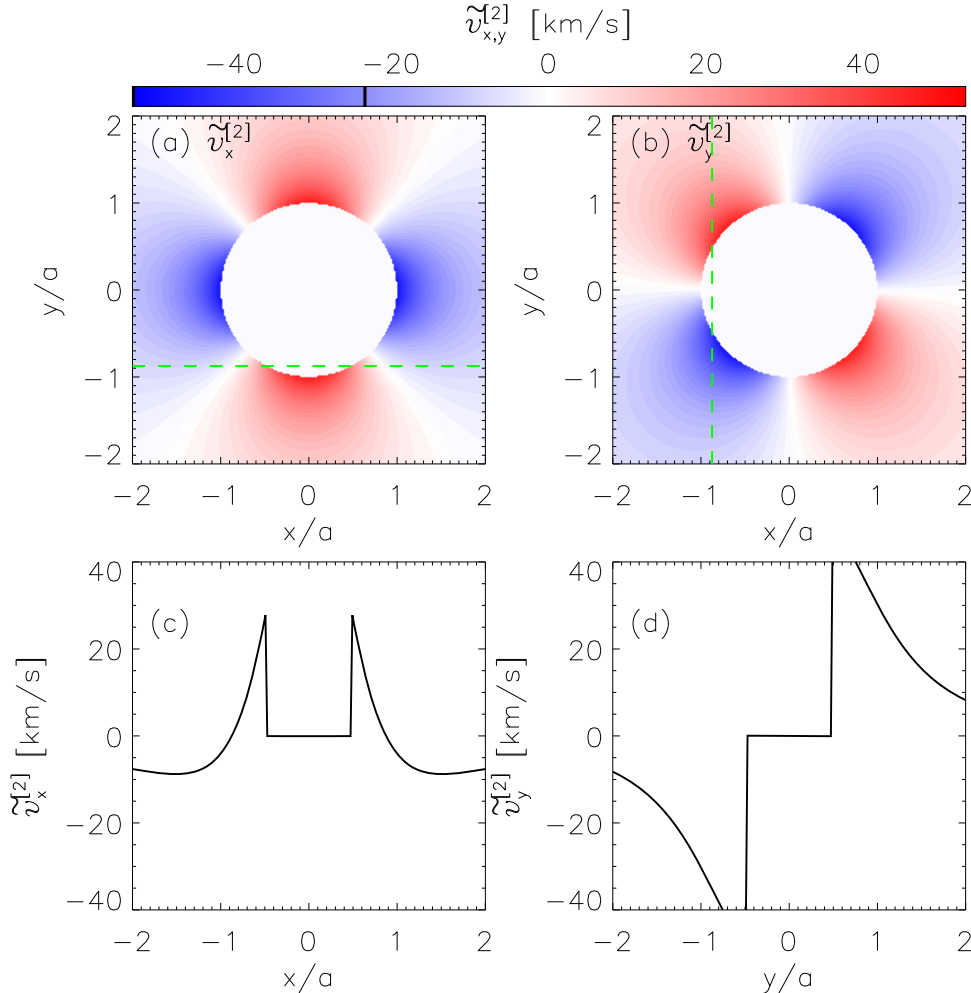\tag{56}
$$

Figure 14. (a) and (b) Cross-sectional distribution of the quadrupole terms $\tilde{v}_x^{[2]}$ and $\tilde{v}_y^{[2]}$. (c) Profiles of $\tilde{v}_x^{[2]}$ along the horizontal dashed line marked in (a). (d) Profiles of $\tilde{v}_y^{[2]}$ along the vertical dashed line labeled in (b).

13

$$\tilde{v}_x|_{r=a^+} = \frac{-A_e\,\omega\kappa_{re}}{2\rho_e(\omega^2 - \omega^2_{Ae})}(-K_0(\kappa_{re}a) - K_2(\kappa_{re}a)), \quad (57)$$

$$= \frac{J_1'(|\kappa_{ri}|a)}{K_1'(\kappa_{re}a)}v_{00}(-K_0(\kappa_{re}a) - K_2(\kappa_{re}a)). \quad (58)$$

where we recalled the total pressure balance at $r = a$ and the dispersion relationship (Equation (13)):

$$A_i J_1(|\kappa_{ri}|a) = A_e K_1(\kappa_{re}a) \quad (59)$$

$$\frac{\rho_i(\omega^2_{Ai} - \omega^2)\kappa_{re}}{\rho_e(\omega^2_{Ae} - \omega^2)|\kappa_{ri}|} = \frac{J_1'(|\kappa_{ri}|a)K_1(\kappa_{re}a)}{J_1(|\kappa_{ri}|a)K_1'(\kappa_{re}a)}. \quad (60)$$

If we use the relationships $J_1' = 0.5(J_0 - J_2)$ and $K_1' = -0.5(K_0 + K_2)$ (Olver et al. 2010) then we can verify that $\tilde{v}_x|_{r=a^-} = \tilde{v}_x|_{r=a^+}$ at $\phi = 0$ and π.

If we follow the same procedure and use the relationships ($J_1' = J_1/\eta - J_2$ and $K_1' = K_1/\eta - K_2$, Olver et al. 2010), then we can easily obtain the vertical component:

$$\tilde{v}_y = \begin{cases} -v_{00}J_2 \sin 2\phi, & \text{for } r \leqslant a \\ -\dfrac{J_1'(|\kappa_{ri}|a)}{K_1'(\kappa_{re}a)}v_{00}K_2 \sin 2\phi, & \text{for } r > a. \end{cases} \quad (61)$$

REFERENCES

Anfinogentov, S., Nisticò, G., & Nakariakov, V. M. 2013, A&A, 560, A107
Antolin, P., Okamoto, T. J., De Pontieu, B., et al. 2015, ApJ, 809, 72
Antolin, P., & Van Doorsselaere, T. 2013, A&A, 555, A74
Antolin, P., & Verwichte, E. 2011, ApJ, 736, 121
Antolin, P., Yokoyama, T., & Van Doorsselaere, T. 2014, ApJL, 787, L22
Arregui, I. 2015, RSPTA, 373, 40261
Arregui, I., Oliver, R., & Ballester, J. L. 2012, LRSP, 9, 2
Aschwanden, M. J., & Boerner, P. 2011, ApJ, 732, 81
Aschwanden, M. J., de Pontieu, B., Schrijver, C. J., & Title, A. M. 2002, SoPh, 206, 99
Aschwanden, M. J., Fletcher, L., Schrijver, C. J., & Alexander, D. 1999, ApJ, 520, 880
Aschwanden, M. J., & Nightingale, R. W. 2005, ApJ, 633, 499
Aschwanden, M. J., & Schrijver, C. J. 2011, ApJ, 736, 102
Brooks, D. H., Warren, H. P., Ugarte-Urra, I., & Winebarger, A. R. 2013, ApJL, 772, L19
Chen, F., & Peter, H. 2015, A&A, 581, A137
Chen, Y., Feng, S. W., Li, B., et al. 2011, ApJ, 728, 147
Chen, Y., Song, H. Q., Li, B., et al. 2010, ApJ, 714, 644
Cooper, F. C., Nakariakov, V. M., & Tsiklauri, D. 2003a, A&A, 397, 765
Cooper, F. C., Nakariakov, V. M., & Williams, D. R. 2003b, A&A, 409, 325
De Moortel, I., & Bradshaw, S. J. 2008, SoPh, 252, 101
De Moortel, I., Hood, A. W., Ireland, J., & Walsh, R. W. 2002a, SoPh, 209, 89
De Moortel, I., Ireland, J., Walsh, R. W., & Hood, A. W. 2002b, SoPh, 209, 61
De Moortel, I., & Nakariakov, V. M. 2012, RSPTA, 370, 3193
De Moortel, I., & Pascoe, D. J. 2009, ApJL, 699, L72
De Pontieu, B., Carlsson, M., Rouppe van der Voort, L. H. M., et al. 2012, ApJL, 752, L12
Dere, K. P., Landi, E., Mason, H. E., Monsignori Fossi, B. C., & Young, P. R. 1997, A&AS, 125, 149
DLMS. 2015, NIST Digital Library of Mathematical Functions, http://dlmf.nist.gov/, Release 1.0.9 of 2014-08-29, online companion to Olver et al. (2010)
Doschek, G. A., Mariska, J. T., Warren, H. P., et al. 2007, ApJL, 667, L109
Edwin, P. M., & Roberts, B. 1982, SoPh, 76, 239
Edwin, P. M., & Roberts, B. 1983, SoPh, 88, 179
Erdélyi, R., & Morton, R. J. 2009, A&A, 494, 295
Fang, X., Yuan, D., Van Doorsselaere, T., Keppens, R., & Xia, C. 2015, ApJ, 813, 33
Goossens, M., Andries, J., Soler, R., et al. 2012, ApJ, 753, 111
Goossens, M., Soler, R., Terradas, J., Van Doorsselaere, T., & Verth, G. 2014, ApJ, 788, 9

Gruszecki, M., Nakariakov, V. M., & Van Doorsselaere, T. 2012, A&A, 543, A12
Guo, Y., Ding, M. D., & Chen, P. F. 2015, ApJS, 219, 36
He, J., Marsch, E., Tu, C., & Tian, H. 2009, ApJL, 705, L217
Hershaw, J., Foullon, C., Nakariakov, V. M., & Verwichte, E. 2011, A&A, 531, A53
Heyvaerts, J., & Priest, E. R. 1983, A&A, 117, 220
Hood, A. W., Browning, P. K., & van der Linden, R. A. M. 2009, A&A, 506, 913
Jess, D. B., Morton, R. J., Verth, G., et al. 2015, SSRv, 190, 103
Kim, S., Nakariakov, V. M., & Cho, K.-S. 2014, ApJL, 797, L22
Klimchuk, J. A. 2006, SoPh, 234, 41
Kumar, P., Innes, D. E., & Inhester, B. 2013, ApJL, 779, L7
Kumar, P., Nakariakov, V. M., & Cho, K.-S. 2015, ApJ, 804, 4
Kuridze, D., Morton, R. J., Erdélyi, R., et al. 2012, ApJ, 750, 51
Kuznetsov, A. A., Van Doorsselaere, T., & Reznikova, V. E. 2015, SoPh, 290, 1173
Lee, H., Moon, Y.-J., & Nakariakov, V. M. 2015, ApJL, 803, L7
Lin, Y., Engvold, O., Rouppe van der Voort, L. H. M., & van Noort, M. 2007, SoPh, 246, 65
Lin, Y., Soler, R., Engvold, O., et al. 2009, ApJ, 704, 870
Liu, W., Nitta, N. V., Schrijver, C. J., Title, A. M., & Tarbell, T. D. 2010, ApJL, 723, L53
Liu, W., & Ofman, L. 2014, SoPh, 289, 3233
Liu, W., Ofman, L., Nitta, N. V., et al. 2012, ApJ, 753, 52
Morton, R. J. 2014, A&A, 566, A90
Morton, R. J., & McLaughlin, J. A. 2013, A&A, 553, L10
Morton, R. J., Tomczyk, S., & Pinto, R. 2015, NatCo, 6, 7813
Nakariakov, V. M., Aschwanden, M. J., & van Doorsselaere, T. 2009, A&A, 502, 661
Nakariakov, V. M., & Ofman, L. 2001, A&A, 372, L53
Nakariakov, V. M., Ofman, L., Deluca, E. E., Roberts, B., & Davila, J. M. 1999, Sci, 285, 862
Nakariakov, V. M., & Verwichte, E. 2005, LRSP, 2, 3
Nisticò, G., Anfinogentov, S., & Nakariakov, V. M. 2014a, A&A, 570, A84
Nisticò, G., Nakariakov, V. M., & Verwichte, E. 2013, A&A, 552, A57
Nisticò, G., Pascoe, D. J., & Nakariakov, V. M. 2014b, A&A, 569, A12
Ofman, L., & Thompson, B. J. 2002, ApJ, 574, 440
Okamoto, T. J., Antolin, P., De Pontieu, B., et al. 2015, ApJ, 809, 71
Okamoto, T. J., & De Pontieu, B. 2011, ApJL, 736, L24
Olver, F. W. J., Lozier, D. W., Boisvert, R. F., & Clark, C. W. (ed.) 2010, NIST Handbook of Mathematical Functions (New York, NY; Cambridge Univ. Press)
O'Shea, E., Srivastava, A. K., Doyle, J. G., & Banerjee, D. 2007, A&A, 473, L13
Pascoe, D. J., Hood, A. W., de Moortel, I., & Wright, A. N. 2012, A&A, 539, A37
Pascoe, D. J., Nakariakov, V. M., & Kupriyanova, E. G. 2013, A&A, 560, A97
Pascoe, D. J., Wright, A. N., & De Moortel, I. 2010, ApJ, 711, 990
Pascoe, D. J., Wright, A. N., & De Moortel, I. 2011, ApJ, 731, 73
Peter, H., Bingert, S., Klimchuk, J. A., et al. 2013, A&A, 556, A104
Reale, F. 2014, LRSP, 11, 4
Reznikova, V. E., Antolin, P., & Van Doorsselaere, T. 2014, ApJ, 785, 86
Reznikova, V. E., Van Doorsselaere, T., & Kuznetsov, A. A. 2015, A&A, 575, A47
Ruderman, M. S. 2003, A&A, 409, 287
Ruderman, M. S. 2009, A&A, 506, 885
Ruderman, M. S., & Erdélyi, R. 2009, SSRv, 149, 199
Ruderman, M. S., & Roberts, B. 2002, ApJ, 577, 475
Schrijver, C. J., Aschwanden, M. J., & Title, A. M. 2002, SoPh, 206, 69
Scullion, E., Rouppe van der Voort, L., Wedemeyer, S., & Antolin, P. 2014, ApJ, 797, 36
Selwa, M., Murawski, K., Solanki, S. K., & Ofman, L. 2010, A&A, 512, A76
Selwa, M., Murawski, K., Solanki, S. K., & Wang, T. J. 2007, A&A, 462, 1127
Selwa, M., Solanki, S. K., & Ofman, L. 2011, ApJ, 728, 87
Thurgood, J. O., Morton, R. J., & McLaughlin, J. A. 2014, ApJL, 790, L2
Tomczyk, S., McIntosh, S. W., Keil, S. L., et al. 2007, Sci, 317, 1192
Tripathi, D., Isobe, H., & Jain, R. 2009, SSRv, 149, 283
Van Doorsselaere, T., Andries, J., Poedts, S., & Goossens, M. 2004, ApJ, 606, 1223
Van Doorsselaere, T., Gijsen, S. E., Andries, J., & Verth, G. 2014, ApJ, 795, 18
Van Doorsselaere, T., & Nakariakov, V. M. 2008, in ASP Conf. Ser. 397, First Results From Hinode, ed. S. A. Matthews, J. M. Davis, & L. K. Harra (San Francisco, CA: ASP), 58

Van Doorsselaere, T., Nakariakov, V. M., & Verwichte, E. 2008, ApJL, 676, L73

Van Doorsselaere, T., Verwichte, E., & Terradas, J. 2009, SSRv, 149, 299

Verwichte, E., Aschwanden, M. J., Van Doorsselaere, T., Foullon, C., & Nakariakov, V. M. 2009, ApJ, 698, 397

Verwichte, E., Foullon, C., & Nakariakov, V. M. 2006, A&A, 452, 615

Verwichte, E., Foullon, C., & Van Doorsselaere, T. 2010, ApJ, 717, 458

Verwichte, E., Nakariakov, V. M., & Cooper, F. C. 2005, A&A, 430, L65

Verwichte, E., Nakariakov, V. M., Ofman, L., & Deluca, E. E. 2004, SoPh, 223, 77

Verwichte, E., Van Doorsselaere, T., Foullon, C., & White, R. S. 2013a, ApJ, 767, 16

Verwichte, E., Van Doorsselaere, T., White, R. S., & Antolin, P. 2013b, A&A, 552, A138

Wang, T. J., Ofman, L., & Davila, J. M. 2009a, ApJ, 696, 1448

Wang, T. J., Ofman, L., Davila, J. M., & Mariska, J. T. 2009b, A&A, 503, L25

Wang, T. J., & Solanki, S. K. 2004, A&A, 421, L33

White, R. S., & Verwichte, E. 2012, A&A, 537, A49

White, R. S., Verwichte, E., & Foullon, C. 2012, A&A, 545, A129

Winebarger, A. R., Warren, H., van Ballegooijen, A., DeLuca, E. E., & Golub, L. 2002, ApJL, 567, L89

Yuan, D., & Nakariakov, V. M. 2012, A&A, 543, A9

Yuan, D., Pascoe, D. J., Nakariakov, V. M., Li, B., & Keppens, R. 2015a, ApJ, 799, 221

Yuan, D., Shen, Y., Liu, Y., et al. 2013, A&A, 554, A144

Yuan, D., & Van Doorsselaere, T. 2016, ApJS, 223, 24

Yuan, D., Van Doorsselaere, T., Banerjee, D., & Antolin, P. 2015b, ApJ, 807, 98

Zimovets, I. V., & Nakariakov, V. M. 2015, A&A, 577, A4